nature geoscience

Article

https://doi.org/10.1038/s41561-024-01444-y

Hydrothermal flow and serpentinization in oceanic core complexes controlled by mafic intrusions

Received: 25 October 2023

Accepted: 5 April 2024

Published online: 06 May 2024

Check for updates

Hanchao Jian [1] ✉, J. Pablo Canales [1] ✉, Robert Dunn [2] & Mladen R. Nedimović [3]

Deep-sea hydrothermal systems at slow/ultraslow-spreading mid-ocean ridges are often located within ultramafic rocks that are part of oceanic core complexes. These complexes contain lower-crustal and mantle sections exhumed due to detachment faulting. Hydrothermal circulation in these environments leads to massive sulfide deposits, hydration of oceanic lithosphere and conditions resembling early Earth's life origin. However, the relationship between hydrothermal pathways in these environments and crustal and mantle lithologies, faulting, magmatism, serpentinization and alteration is poorly understood. Here we present seismic models of a Mid-Atlantic Ridge core complex and its ultramafic-hosted hydrothermal system derived from full waveform inversion of controlled-source seismic data and from local earthquake tomography. The models and derived rock properties reveal high-permeability channels within serpentinized peridotite along the flanks of the core complex. These channels converge beneath active and fossil hydrothermal fields and are diverted around mechanically strong, impermeable shallow mafic intrusions (2–3 km wide, ~1 km thick), causing hydrothermal outflow and the formation of massive sulfide deposits around the intrusions' edges. These mafic intrusions also act as lids that limit fluid downflow—and thus serpentinization—in the centre of the core complex. Our results demonstrate that hydrothermal flow in ultramafic settings is controlled by lithology contacts, with mafic intrusions modulating hydrothermal pathways and extent of mantle serpentinization at depth.

Hydrothermal circulation at mid-ocean ridges (MORs) accounts for ~10% of total heat loss of oceanic plates[1]. Hydrothermal systems host macrobiota and chemosynthetic microbial communities[2] and form seafloor massive sulfide (SMS) deposits[3]. At slow/ultraslow-spreading MORs, lithospheric heterogeneity resulting from temporal and spatial variations in magmatic, tectonic and alteration processes gives rise to a variety of hydrothermal systems classified as[4]: type I, hosted in volcanic terrain, driven by magmatic heat and characterized by high-temperature (high-T) and acidic fluids, enriched in magmatically derived CO_2 relative to seawater and variable concentrations of H_2 and CH_4; type II, hosted in a mixture of gabbroic and ultramafic material venting CO_2-rich fluids with elevated concentrations of H_2, CH_4 and other hydrocarbons indicative of serpentinization; and type III, low-temperature (low-T), peridotite-hosted systems where fluid

[1]Department of Geology and Geophysics, Woods Hole Oceanographic Institution, Woods Hole, MA, USA. [2]Department of Earth Sciences, School of Ocean and Earth Science and Technology, University of Hawai'i at Mānoa, Honolulu, HI, USA. [3]Department of Earth and Environmental Sciences, Dalhousie University, Halifax, Nova Scotia, Canada. ✉e-mail: hjian@whoi.edu; jcanales@whoi.edu

https://doi.org/10.1038/s41561-024-01444-y

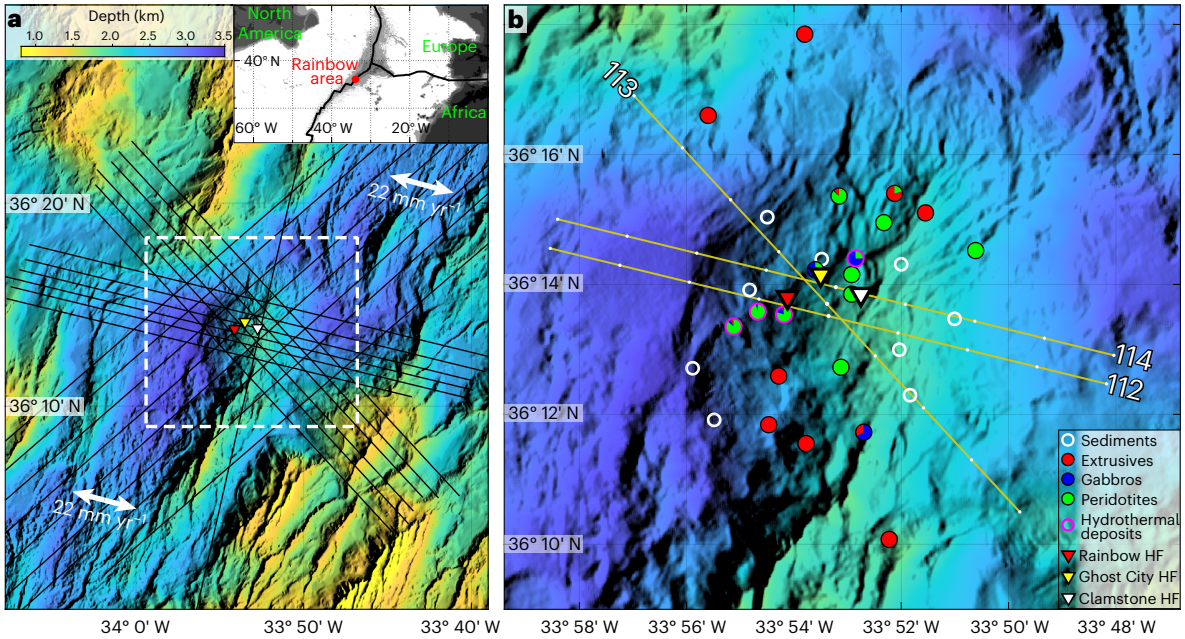

Fig. 1 | Bathymetry map and multichannel seismic layout. a, Regional bathymetry[19] and multichannel seismic profiles (black lines) across the Rainbow non-transform offset and neighbouring segments. White arrows and numbers show full spreading direction and rate. The inset shows the location of the study area (red dot) within the central North Atlantic Ocean. White box outlines the area shown in **b**. **b**, Bathymetry and dredged lithologies[21] of the Rainbow massif. The brown lines are the multichannel seismic profile sections shown in Fig. 2 and Extended Data Figs. 4 and 5, with small white dots marking inline distances at every 2 km.

circulation is driven predominantly by cooling and serpentinization of mantle material and where fluids exiting carbonate chimneys are CO_2-poor but enriched in H_2, CH_4 and other hydrocarbons of abiogenic origin.

Type I systems share many of the characteristics of fast-spreading systems[4], but types II and III, collectively known as ultramafic-hosted systems, appear to be exclusive of slow/ultraslow-spreading MORs, with nearly all of the known cases being associated with oceanic core complexes (OCCs)[5]. High-T and low-T hydrothermal systems—both active and fossil, on-axis and off-axis—are common in OCCs[6,7], indicating that hydrothermal circulation is a fundamental process that accompanies tectonic and magmatic activity throughout the life cycle of an OCC[8]. However, our knowledge of how crustal and mantle lithologies, rock hydration and alteration, faulting and magmatism collectively determine hydrothermal pathways in these settings is limited, hindering progress on understanding of the importance of OCCs and associated hydrothermal circulation for the formation of SMS ore deposits, for hydration of young lithosphere and for creating chemical and structural environments potentially analogous to those that facilitated the origin of life on early Earth[2].

Modelling hydrothermal flow in these complex settings has been restricted to investigating the role of some particular features, such as the geometry and permeability of faults in focusing hydrothermal discharge[9], or the feedbacks between permeability and serpentinization[10]. The few seismic studies conducted to date in OCCs with type II or type III systems provide first-order constraints on crustal structure[11,12] but lack the resolution for adequately addressing how hydrothermal circulation is influenced by a complex, heterogeneous lithological and alteration structure. Furthermore, because P-wave velocity (V_P) is influenced by a variety of factors such as composition, alteration, porosity and pore space topology, distinguishing among these factors from V_P alone is in many cases problematic and requires additional constraints such as shear-wave velocity (V_S) or the V_P/V_S ratio[13]. Advanced seismic imaging such as full waveform inversion (FWI) of controlled-source seismic data has the potential to illuminate structures at scales adequate for linking seafloor observations of hydrothermal discharge with sub-seafloor structures[14,15], and the fine-scale V_P/V_S structure derived from microearthquake data[16] could provide the necessary constraints for distinguishing the roles of lithology, porosity and serpentinization in controlling hydrothermal circulation. In this study, application of these high-resolution imaging methods on datasets from the Rainbow massif[11,17–19] (Methods) reveals that type II–III hydrothermal systems are controlled by mafic intrusions that modulate fluid pathways at depth, location of outflow zones on the seafloor and extent of serpentinization.

The Rainbow massif

The Rainbow massif is an ultramafic OCC located in a non-transform offset of the Mid-Atlantic Ridge[20] (Fig. 1a). Basement outcrops at the centre of the massif expose predominately serpentinites with sporadic gabbros, while basalts have been recovered only around its edges[21] (Fig. 1b). The massif hosts the Rainbow hydrothermal field (HF), a well-studied type II active system venting ~365 °C, H_2-rich, CH_4-rich, CO_2-rich and Fe-rich fluids[22] at high heat and volume fluxes[23] that has been active for ~23 kyr (ref. 24) and is associated with one of the most extensive active polymetallic SMS deposits found at MORs[3,25]. Two fossil hydrothermal fields, ~110 kyr-old Ghost City and ~25.5 kyr-old Clamstone, located 1.2 km and 2.5 km from the Rainbow HF, respectively, show characteristics typical of type III systems, such as low-T, metal-poor and alkaline vent fluids[4,26,27]. Additional hydrothermal outflow zones are inferred from mineralized rock samples[21] (Fig. 1b).

A previous seismic study shows that the massif is characterized by thin seismic crust (defined as $V_P \leq 7.2$ km s^{-1}) and a cone-shaped core of high V_P (reaching 6.0–7.2 km s^{-1} at 1–2 km below seafloor (b.s.f.)) capped by shallow low-V_P flanks[11]. Seismic reflection images reveal reflectors beneath the flanks of the massif dipping away from the summit and short, sub-horizontal reflectors broadly distributed throughout the massif interpreted as solidified and possibly partially molten magmatic sills intruding ultramafic rocks[17]. The massif is inferred to be deformed by some combination of tectonic extension, thermal contraction and

https://doi.org/10.1038/s41561-024-01444-y

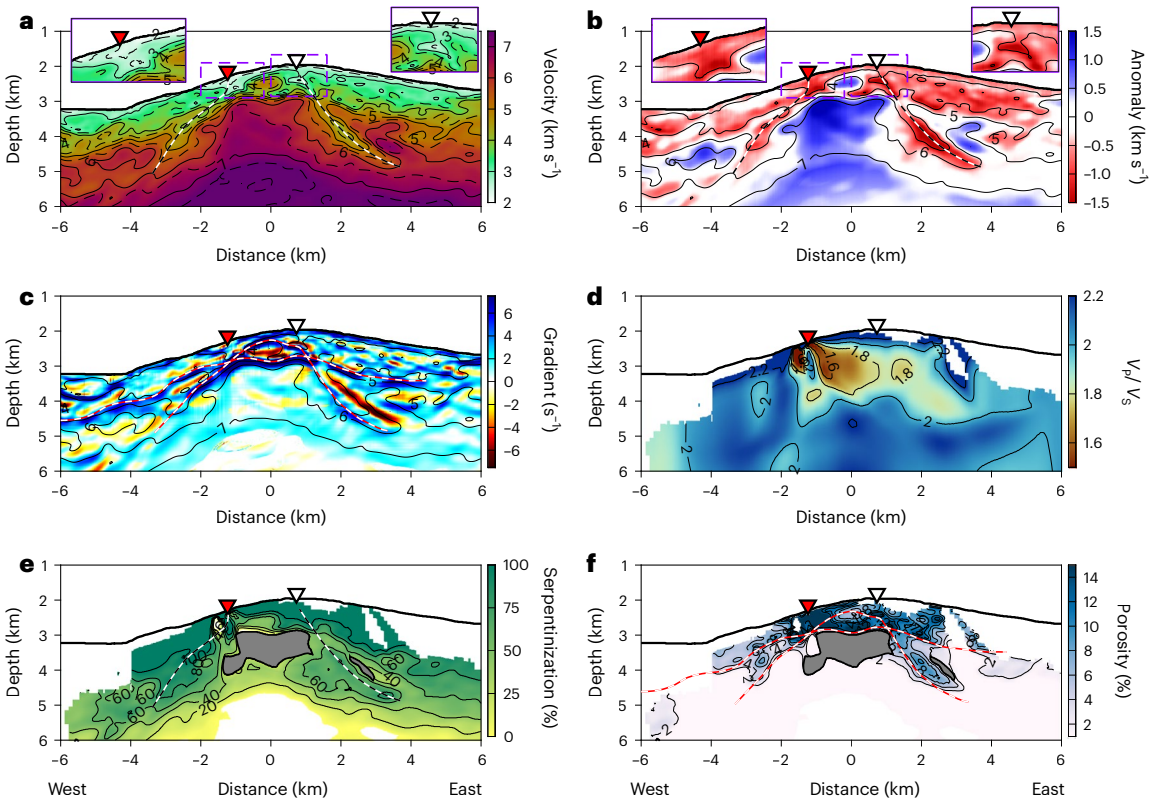

Fig. 2 | Geophysical cross sections along profile 112. a–**c**, V_P (**a**), V_P anomalies (**b**) and V_P gradients (amplitude of total spatial gradient combined with the sign of vertical gradient) (**c**) derived from the FWI of multichannel seismic data. Labelled black contours in **a**–**c** all correspond to the V_P model in **a**. **d**, V_P/V_S ratios derived from the local earthquake tomography. **e**,**f**, Preferred estimates of degree of serpentinization (**e**) and porosity (**f**) from effective medium theory consistent with the [V_P, V_P/V_S] results in **a** and **d** (Methods). Inverted triangles are projected locations of hydrothermal fields as shown in Fig. 1b. The insets in **a** and **b** show zoomed-in plots of the shallow low-V_P zones associated with the hydrothermal fields. Black-and-white dashed lines on **a**, **b** and **e** delineate low-V_P channels as interpreted in **b**. Red-and-white dashed lines on **c** and **f** delineate high-V_P gradients as interpreted in **c**. The dark grey patches on **e** and **f** mark interpreted gabbro-dominant regions.

serpentinization-driven volume expansion, as suggested by a high constant rate of low-magnitude, shallow microseismicity (<4 km b.s.f.) lacking mainshock–aftershock sequences or swarming activity[18].

Hydrothermal pathways and mafic intrusions

Seismic velocity models derived from the FWI of downward-extrapolated multichannel seismic data (Extended Data Figs. 1–3 and Methods) illuminate the high-V_P core of the massif bounded by sharp transitions on its top and sides, accompanied by dipping low-V_P channels along the flanks (Fig. 2a–c and Extended Data Figs. 4a–c and 5a–c). These channels extend from near the seafloor in the immediate vicinity of the known hydrothermal fields to depths greater than 5 km below sea level. This geometry suggests that the low-V_P channels represent hydrothermal pathways that focus fluids heated from deep, partially molten sills[17] to a narrow region at the centre of the massif. Alternative interpretations of these narrow low-V_P anomalies based on temperature or presence of melt[28] would require too large temperature gradients and large amounts of partial melt that we deem unrealistic. The low-V_P channels beneath the western flank of the massif converge beneath the Rainbow HF and are therefore highly permeable active upflow zones. By contrast, channels beneath the eastern flank of the massif converge beneath the fossil Clamstone HF and are inferred to be inactive because of a decrease in permeability due to clogging of pore space by low-V_P alteration products (for example, serpentinites) and/or because of waning of a local heat source. At the top of the low-V_P channels and immediately beneath the hydrothermal fields, the FWI models exhibit ~300–1,000 m wide low-V_P zones in the upper few hundred metres (Fig. 2a,b and Extended Data Figs. 4a,b and 5a,b). We interpret these shallow low-V_P zones as sub-seafloor brecciated stockwork assemblages, in agreement with the extent of the Rainbow HF stockwork inferred from seafloor samples[25] and the internal structure of other SMS deposits inferred from drilling[29].

The V_P/V_S ratio obtained from a local earthquake tomography (Extended Data Fig. 6 and Methods) provides independent constraints for distinguishing between ultramafic and mafic lithologies[13,30]. Cross sections of the V_P/V_S volume coincident with the FWI V_P models show that while the Rainbow massif generally exhibits $V_P/V_S > 1.9$ indicative of serpentinization[13] and consistent with the overall ultramafic nature of the massif, there is important variability (Fig. 2d and Extended Data Figs. 4d and 5d). Most prominent is a region of low V_P/V_S located westwards of the summit above ~3.5–4.0 km depth below sea level. This region overlaps the upper section of the high-V_P core, strongly suggesting the presence of gabbro intrusions. Statistical analysis of existing laboratory and in situ measurements of seismic properties for mafic and ultramafic lithologies (Extended Data Fig. 7) indicates that high-concentration gabbro intrusions can be identified using $V_P > 5.5$ km s^{-1} and $V_P/V_S < 1.85$ (Methods). Using these criteria, a gabbro-dominant region (2–3 km wide, ~1 km thick) at shallow depths beneath the summit of the Rainbow massif is interpreted from the seismic models (grey shaded regions in Fig. 2 and Extended Data Figs. 4 and 5). It is comparable in size to other seismically imaged and/or drilled OCC gabbroic cores (for example, refs. 14,31,32), which probably formed deeper into the lithosphere and were subsequently uplifted through detachment faulting[21,33].

The upper sections of the low-V_P channels run beside the borders of this gabbro-dominant region, and the known HFs are located roughly

https://doi.org/10.1038/s41561-024-01444-y

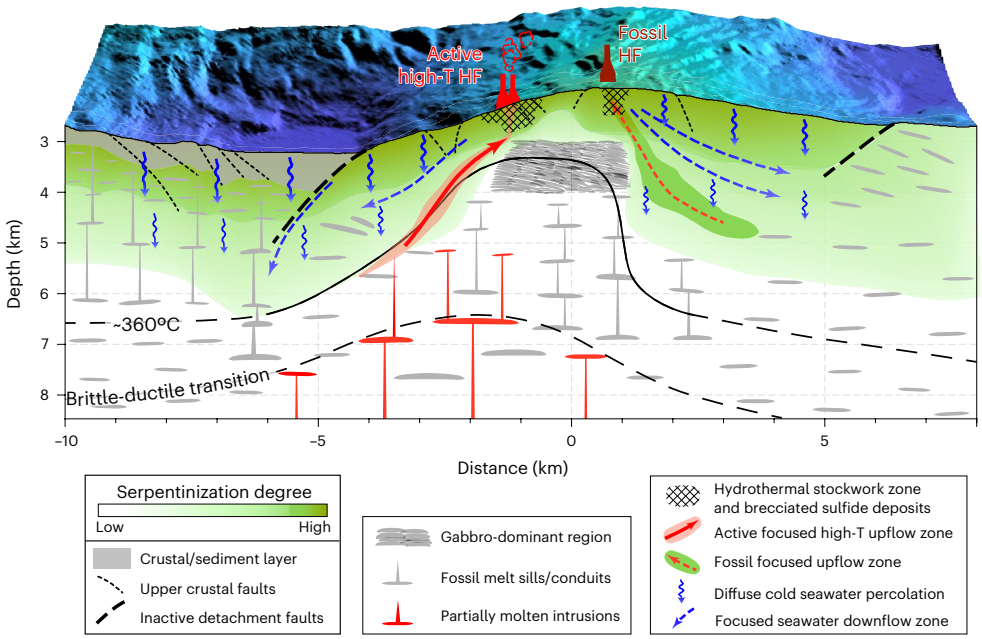

Fig. 3 | Schematic model for hydrothermal circulation and serpentinization in ultramafic OCCs. The gabbro-dominant region acts as a barrier to extensive fluid downflow into the core of the OCC, sheltering it from extensive convective cooling and serpentinization. Magmatic sills intrude into ultramafic rocks throughout the OCC[17], and those intruding in the warmer core of the OCC are more slowly cooled. Localized strains around the lithology contact form focused hydrothermal outflow pathways, leading to the formation of hydrothermal fields located around the vertical projection of the gabbro-dominant region's edges. Figure adapted with permission from ref. 11, John Wiley and Sons.

around the edges of this region when projected to the seafloor (Fig. 2e and Extended Data Figs. 4e and 5e). These observations indicate that the mafic intrusions control the hydrothermal outflow zones in these settings by providing a rheological contrast that favours nucleation and development of fractures between the low-permeability, mechanically strong mafic rocks and the weak serpentinized peridotites[34] around it as well as other weak alteration minerals formed in response to strain localization and hydrothermal alteration during denudation[8].

Extent of serpentinization

We use effective medium theory and constraints from lab measurements to explore the range of porosity, crack aspect ratio and serpentinization structures that are consistent with our V_P and V_P/V_S models (Extended Data Fig. 8 and Methods). Although solutions are not unique, in this Article, we report on the endmember solution that results in the maximum extent of serpentinization allowed by the data. We consider these our preferred porosity and serpentinization models for two reasons. First, the preferred serpentinization models (Fig. 2e and Extended Data Figs. 4e and 5e) are the most geologically plausible as indicated by the complete serpentinization of seafloor samples[21,25]. Second, the preferred solution consists of an ~1 km thick high-porosity uppermost layer (Fig. 2f and Extended Data Figs. 4f and 5f), in which porosity, crack aspect ratio (Extended Data Fig. 9b) and a sharp porosity reduction at its base are all comparable to drilling results in ophiolitic serpentinized mantle[35]. The sharp porosity reduction also explains the high FWI–V_P-gradient boundaries. Solutions with lower extents of serpentinization (for example, Extended Data Fig. 9d–i), while compatible with our V_P and V_P/V_S models, are inconsistent with the extent of serpentinization in seafloor samples[21] and require a gradual (rather than a sharp) decrease in porosity with depth that conflicts with the modelled FWI V_P gradients.

Our preferred serpentinization models show that the high-porosity upper ~1 km of the massif is almost completely serpentinized (>80%) (Fig. 2e and Extended Data Figs. 4e and 5e). Deeper within the massif, serpentinization varies laterally, with the low-V_P channels displaying ~60% serpentinization while the area below the gabbro-dominant region is characterized by less-altered peridotites (<40%). This reinforces our interpretation of the low-V_P channels as fluid pathways, and it highlights the role that the mafic intrusions play in controlling alteration of the massif. Gabbros are strong materials resistant to retrograde metamorphism[21] and would remain relatively intact and less permeable than serpentinized peridotites during exhumation[36]. Therefore, we posit that the mafic intrusions act as a low-permeability barrier that prevents extensive fluid circulation beneath it, thus limiting the hydration within the central core of the OCC (Fig. 3). Such a barrier to fluid downflow may also help maintain a warmer thermal regime than the surrounding rock by reducing convective cooling, consistent with the presence of partially molten sills imaged beneath the gabbro-dominant region[17], thus further limiting the extent of hydration by damping serpentinization reaction kinetics, which sharply decreases for temperatures above ~320 °C (ref. 37).

Fluid flow in ultramafic settings and global implications

Detachment faulting is a fundamental mode of lithospheric accretion that may comprise up to 50% of slow-spreading and about 40% of ultraslow-spreading lithosphere[38–40]. OCCs formed by this mechanism are systematically characterized by kilometre-scale exhumed mafic intrusions as revealed by seismic investigations and deep drilling (for example, refs. 14,31,32) and host the majority of known ultramafic-hosted hydrothermal systems[5,7]. Therefore, our results from the Rainbow massif can be synthesized into a general model of hydrothermal circulation and serpentinization in OCCs that is representative of these features along slow/ultraslow-spreading ridges, which comprise ~50% of the global MOR system[40].

In our model, large mafic intrusions formed during active detachment faulting and uplifted to shallow levels act as one of the two primary controls in modulating hydrothermal fluid flow and mantle serpentinization; the other primary control is availability of adjacent magmatic heat sources to drive hydrothermal convection[17] (Fig. 3). The mechanically strong and less permeable gabbros prevent substantial fluid downflow into the core of the OCC, thus sheltering it from

extensive serpentinization and providing a warmer thermal regime beneath the gabbro-dominant region. By contrast, fluid downflow and serpentinization are favoured down the flanks of the OCC, creating dipping high-permeability channels within highly serpentinized peridotite. The warmer thermal regime beneath the large shallow mafic region facilitates intrusion of younger, deep-sourced magmatic sills[17]. When these sills are intruded in the vicinity of the channels, deep heated fluids exploit these channels as preferential outflow zones, leading to further alteration and focusing of fluids along the channels[8,41] (Fig. 3). At shallow levels, hydrothermal outflow is focused beside the borders of the gabbro-dominant region favoured by the rheological contrast between weak serpentines and gabbros, leading to the formation of hydrothermal fields and SMS deposits that are not randomly distributed on the seafloor but instead are located around the vertical projection of the edges of the gabbro-dominant region (Fig. 3).

The similarities in structure beneath the Rainbow and the Clamstone HFs suggest that the characteristics of hydrothermal activity at Clamstone was at some point in the past similar to that of the Rainbow HF. As pore space within the focused upflow zones gets clogged due to mineral precipitation and/or serpentinization-induced volume expansion[42], and/or the magmatic heat source wanes or shifts away, hydrothermal outflow may be suppressed, leading to the evolution from a type II to a type III hydrothermal system, which eventually would become inactive. Thus, type II and type III hydrothermal systems probably represent different evolutionary stages of a single ultramafic-hosted style of hydrothermal convection. This further implies that SMS deposits can probably be found beneath both types of systems, as indicated by the similar low-V_P stockwork zones imaged beneath the Rainbow and Clamstone HFs (Fig. 2b).

These results and models thus provide insight into the geophysical and geological environments influencing SMS deposit formation and preservation. Such characterization is crucial for developing sustainable and responsible management and mitigating strategies in the event these systems were to be commercially exploited by deep-sea mining, a scenario potentially having long-lasting ecological and environmental impacts[43] that could become reality in coming years[44].

Furthermore, serpentinization of oceanic lithosphere plays a key role in global carbon and water cycles[45] and serves as a notable source of molecular hydrogen and abiotic methane[40,46], which in turn has important implications for subduction zone processes, mantle rheology, climate stability and the life origin on early Earth, as well as the functioning of the present-day deep biosphere[45–48]. For example, during the past ~320 Myr, global subduction of serpentine-rich oceanic lithosphere has episodically peaked over the last 100 Myr, driven by serpentinization associated with slow/ultraslow seafloor spreading following supercontinent break-up[45,46] and subduction during the closing of internal oceans[49]. Our results indicate that extensive serpentinization (>20%) at OCCs is limited to the upper ~3–4 km of the lithosphere, contrasting with recent claims that oceanic lithosphere hydration at MORs may extend ~30 km into the mantle, at least locally beneath transform faults[50]. Thus, our estimates on the extent of serpentinization at OCCs should be considered when quantifying past, present and future global volatile fluxes.

Online content

Any methods, additional references, Nature Portfolio reporting summaries, source data, extended data, supplementary information, acknowledgements, peer review information; details of author contributions and competing interests; and statements of data and code availability are available at https://doi.org/10.1038/s41561-024-01444-y.

References

1. Stein, C. A. & Stein, S. Constraints on hydrothermal heat flux through the oceanic lithosphere from global heat flow. *J. Geophys. Res. Solid Earth* **99**, 3081–3095 (1994).
2. Martin, W., Baross, J., Kelley, D. & Russell, M. J. Hydrothermal vents and the origin of life. *Nat. Rev. Microbiol.* **6**, 805–814 (2008).
3. German, C. R., Petersen, S. & Hannington, M. D. Hydrothermal exploration of mid-ocean ridges: where might the largest sulfide deposits be forming? *Chem. Geol.* **420**, 114–126 (2016).
4. Früh-Green, G. L. et al. Diversity of magmatism, hydrothermal processes and microbial interactions at mid-ocean ridges. *Nat. Rev. Earth Environ.* **3**, 852–871 (2022).
5. Fouquet, Y. et al. in *Diversity of Hydrothermal Systems on Slow Spreading Ocean Ridges* (eds Rona, P. A. et al.) 321–367 (AGU, 2010); https://doi.org/10.1029/2008GM000746
6. McCaig, A. M., Cliff, R. A., Escartin, J., Fallick, A. E. & MacLeod, C. J. Oceanic detachment faults focus very large volumes of black smoker fluids. *Geology* **35**, 935–938 (2007).
7. Kim, J. et al. Discovery of active hydrothermal vent fields along the Central Indian Ridge, 8–12° S. *Geochem. Geophys. Geosyst.* **21**, e2020GC009058 (2020).
8. Picazo, S. et al. Deformation associated with the denudation of mantle-derived rocks at the Mid-Atlantic Ridge 13°–15° N: the role of magmatic injections and hydrothermal alteration. *Geochem. Geophys. Geosyst.* **13**, Q04G09 (2012).
9. Guo, Z. et al. Detachment-parallel recharge can explain high discharge fluxes at the TAG hydrothermal field. *Earth Planet. Sci. Lett.* **617**, 118245 (2023).
10. Iyer, K., Rüpke, L. H. & Morgan, J. P. Feedbacks between mantle hydration and hydrothermal convection at ocean spreading centers. *Earth Planet. Sci. Lett.* **296**, 34–44 (2010).
11. Dunn, R. A., Arai, R., Eason, D. E., Canales, J. P. & Sohn, R. A. Three-dimensional seismic structure of the Mid-Atlantic Ridge: an investigation of tectonic, magmatic, and hydrothermal processes in the Rainbow area. *J. Geophys. Res. Solid Earth* **122**, 9580–9602 (2017).
12. Harding, J. L. et al. Magmatic–tectonic conditions for hydrothermal venting on an ultraslow-spread oceanic core complex. *Geology* **45**, 839–842 (2017).
13. Grevemeyer, I. et al. Episodic magmatism and serpentinized mantle exhumation at an ultraslow-spreading centre. *Nat. Geosci.* **11**, 444–448 (2018).
14. Harding, A. J., Arnulf, A. F. & Blackman, D. K. Velocity structure near IODP Hole U1309D, Atlantis massif, from waveform inversion of streamer data and borehole measurements. *Geochem. Geophys. Geosyst.* **17**, 1990–2014 (2016).
15. Marjanović, M., Barreyre, T., Fontaine, F. J. & Escartín, J. Investigating fine-scale permeability structure and its control on hydrothermal activity along a fast-spreading ridge (the East Pacific Rise, 9°43′–53′ N) using seismic velocity, poroelastic response, and numerical modeling. *Geophys. Res. Lett.* **46**, 11799–11810 (2019).
16. Baillard, C., Wilcock, W. S. D., Arnulf, A. F., Tolstoy, M. & Waldhauser, F. A joint inversion for three-dimensional P and S wave velocity structure and earthquake locations beneath Axial seamount. *J. Geophys. Res. Solid Earth* **124**, 12997–13020 (2019).
17. Canales, J. P., Dunn, R. A., Arai, R. & Sohn, R. A. Seismic imaging of magma sills beneath an ultramafic-hosted hydrothermal system. *Geology* **45**, 451–454 (2017).
18. Horning, G., Sohn, R. A., Canales, J. P. & Dunn, R. A. Local seismicity of the Rainbow massif on the Mid-Atlantic Ridge. *J. Geophys. Res. Solid Earth* **123**, 1615–1630 (2018).
19. Paulatto, M., Canales, J. P., Dunn, R. A. & Sohn, R. A. Heterogeneous and asymmetric crustal accretion: new constraints from multibeam bathymetry and potential field data from the Rainbow area of the Mid-Atlantic Ridge (36°15′ N). *Geochem. Geophys. Geosyst.* **16**, 2994–3014 (2015).
20. Gràcia, E., Charlou, J. L., Radford-Knoery, J. & Parson, L. M. Non-transform offsets along the Mid-Atlantic Ridge south of the Azores (38° N–34° N): ultramafic exposures and hosting of hydrothermal vents. *Earth Planet. Sci. Lett.* **177**, 89–103 (2000).

21. Andreani, M. et al. Tectonic structure, lithology, and hydrothermal signature of the Rainbow massif (Mid-Atlantic Ridge 36°14′ N). *Geochem. Geophys. Geosyst.* **15**, 3543–3571 (2014).
22. Charlou, J. L., Donval, J. P., Fouquet, Y., Jean-Baptiste, P. & Holm, N. Geochemistry of high H_2 and CH_4 vent fluids issuing from ultramafic rocks at the Rainbow hydrothermal field (36°14′ N, MAR). *Chem. Geol.* **191**, 345–359 (2002).
23. German, C. R. et al. Heat, volume and chemical fluxes from submarine venting: a synthesis of results from the Rainbow hydrothermal field, 36° N MAR. *Deep Sea Res. 1* **57**, 518–527 (2010).
24. Kuznetsov, V. et al. ^{230}TH/U dating of massive sulfides from the Logatchev and Rainbow hydrothermal fields (Mid-Atlantic Ridge). *Geochronometria* **25**, 51–55 (2006).
25. Marques, A. F. A., Barriga, F., Chavagnac, V. & Fouquet, Y. Mineralogy, geochemistry, and Nd isotope composition of the Rainbow hydrothermal field, Mid-Atlantic Ridge. *Min. Depos.* **41**, 52–67 (2006).
26. Lartaud, F. et al. Fossil clams from a serpentinite-hosted sedimented vent field near the active smoker complex Rainbow, MAR, 36°13′ N: insight into the biogeography of vent fauna. *Geochem. Geophys. Geosyst.* **11**, Q0AE01 (2010).
27. Lartaud, F. et al. Fossil evidence for serpentinization fluids fueling chemosynthetic assemblages. *Proc. Natl Acad. Sci. USA* **108**, 7698–7703 (2011).
28. Dunn, R. A., Toomey, D. R. & Solomon, S. C. Three-dimensional seismic structure and physical properties of the crust and shallow mantle beneath the East Pacific Rise at 9°30′ N. *J. Geophys. Res. Solid Earth* **105**, 23537–23555 (2000).
29. Humphris, S. E. et al. The internal structure of an active sea-floor massive sulphide deposit. *Nature* **377**, 713–716 (1995).
30. Christensen, N. I. Serpentinites, peridotites, and seismology. *Int. Geol. Rev.* **46**, 795–816 (2004).
31. Canales, J. P., Tucholke, B. E., Xu, M., Collins, J. A. & DuBois, D. L. Seismic evidence for large-scale compositional heterogeneity of oceanic core complexes. *Geochem. Geophys. Geosyst.* **9**, Q08002 (2008).
32. Blackman, D. K. et al. Seismic properties of gabbroic sections in oceanic core complexes: constraints from seafloor drilling. *Mar. Geophys. Res.* **40**, 557–569 (2019).
33. Grimes, C. B., John, B. E., Cheadle, M. J. & Wooden, J. L. Protracted construction of gabbroic crust at a slow spreading ridge: constraints from ^{206}Pb/^{238}U zircon ages from Atlantis massif and IODP Hole U1309D (30° N, MAR). *Geochem. Geophys. Geosyst.* **9**, Q08012 (2008).
34. Escartín, J., Hirth, G. & Evans, B. Strength of slightly serpentinized peridotites: implications for the tectonics of oceanic lithosphere. *Geology* **29**, 1023–1026 (2001).
35. Katayama, I. et al. Crack geometry of serpentinized peridotites inferred from onboard ultrasonic data from the Oman Drilling Project. *Tectonophysics* **814**, 228978 (2021).
36. Katayama, I., Terada, T., Okazaki, K. & Tanikawa, W. Episodic tremor and slow slip potentially linked to permeability contrasts at the Moho. *Nat. Geosci.* **5**, 731–734 (2012).
37. Malvoisin, B., Brunet, F., Carlut, J., Rouméjon, S. & Cannat, M. Serpentinization of oceanic peridotites: 2. Kinetics and processes of San Carlos olivine hydrothermal alteration. *J. Geophys. Res. Solid Earth* **117**, B04102 (2012).
38. Escartín, J. et al. Central role of detachment faults in accretion of slow-spreading oceanic lithosphere. *Nature* **455**, 790–794 (2008).
39. Cannat, M. et al. Modes of seafloor generation at a melt-poor ultraslow-spreading ridge. *Geology* **34**, 605–608 (2006).
40. Cannat, M., Fontaine, F. & Escartín, J. in *Diversity of Hydrothermal Systems on Slow Spreading Ocean Ridges* (eds Rona, P. A. et al.) 241–264 (AGU, 2010); https://doi.org/10.1029/2008GM000760
41. Hirose, T. & Hayman, N. W. Structure, permeability, and strength of a fault zone in the footwall of an oceanic core complex, the Central Dome of the Atlantis massif, Mid-Atlantic Ridge, 30° N. *J. Struct. Geol.* **30**, 1060–1071 (2008).
42. Klein, F. & Le Roux, V. Quantifying the volume increase and chemical exchange during serpentinization. *Geology* **48**, 552–556 (2020).
43. Drazen, J. C. et al. Midwater ecosystems must be considered when evaluating environmental risks of deep-sea mining. *Proc. Natl Acad. Sci. USA* **117**, 17455–17460 (2020).
44. Bang, R. N. & Trellevik, L.-K. L. Perspectives on exploration and extraction of seafloor massive sulfide deposits in Norwegian waters. *Min. Econ.* https://doi.org/10.1007/s13563-022-00346-y (2022).
45. Merdith, A. S., Atkins, S. E. & Tetley, M. G. Tectonic controls on carbon and serpentinite storage in subducted upper oceanic lithosphere for the past 320 Ma. *Front. Earth Sci.* **7**, 332 (2019).
46. Merdith, A. S. et al. Pulsated global hydrogen and methane flux at mid-ocean ridges driven by Pangea breakup. *Geochem. Geophys. Geosyst.* **21**, e2019GC008869 (2020).
47. Cooper, G. F. et al. Variable water input controls evolution of the Lesser Antilles volcanic arc. *Nature* **582**, 525–529 (2020).
48. Ménez, B. et al. Abiotic synthesis of amino acids in the recesses of the oceanic lithosphere. *Nature* **564**, 59–63 (2018).
49. Agard, P. Subduction of oceanic lithosphere in the Alps: selective and archetypal from (slow-spreading) oceans. *Earth Sci. Rev.* **214**, 103517 (2021).
50. Wang, Z., Singh, S. C., Prigent, C., Gregory, E. P. M. & Marjanović, M. Deep hydration and lithospheric thinning at oceanic transform plate boundaries. *Nat. Geosci.* **15**, 741–746 (2022).

Methods

Multichannel seismic data acquisition and processing

The multichannel seismic (MCS) dataset was collected in April–May on board the R/V *Marcus G. Langseth*[51]. Twenty-one two-dimensional (2D) MCS profiles were acquired with different orientations (Fig. 1a). The acquisition parameters and full data processing flow are presented in Supplementary Table 1. A crucial step in the processing involved the downward extrapolation of the sea surface data to a virtual datum near the seafloor[52–54], which would migrate the crustal phases ahead of seafloor reflections at near offsets, effectively suppressing seafloor scatterings and enhancing the coherency of wide-angle crustal arrivals (for example, Supplementary Figs. 1–3). We used a 2D Kirchhoff integral method for the extrapolation[55]. The virtual datum was set at 100 m above a smoothed seafloor model, containing virtual sources spaced at 37.5 m and virtual receivers positioned behind sources from 100 m to 8 km. This was applied on all MCS profiles.

Streamer travel-time tomography

To mitigate cycle-skipping issues in FWI, we first performed 3D streamer tomography using first arrival data from all MCS profiles around the Rainbow massif. We picked ~6.99 million travel times with an average uncertainty of 15.8 ms within the tomography model area (43.2 km × 27.9 km; Supplementary Fig. 4a). We adopted the tomography code developed by ref. 56 and added parallelization to handle the large data and model size. It utilizes the shortest-path[57] and LSQR (method for solving least-squares problems using QR factorization at each iteration)[58,59] methods for forward modelling and inversion, respectively. The forward and inversion modelling grids have horizontal by vertical spacing of 37.5 m × 25 m and 150 m × 100 m, respectively. We used the controlled-source ocean-bottom seismometer (OBS) travel-time tomography model[11] as a starting model. The χ^2 (average of squares of the travel-time misfit normalized by picking uncertainties) was 18.5 for the starting model and reduced to ~1 after the streamer tomography (Supplementary Fig. 4b). The cross sections of the streamer tomography model along profiles 112, 114 and 113 (Extended Data Fig. 1a and Supplementary Figs. 5a and 6a) were used as starting models for FWI.

Full waveform inversion

We adopted a 2D time-domain FWI routine[60], which uses the fourth-order staggered-grid finite-difference method[61] for elastic waveform modelling and the adjoint-state method[62] to efficiently calculate the first-order gradient with respect to velocity models. To facilitate the convergence, we incorporated the limited-memory BFGS (Broyden–Fletcher–Goldfarb–Shanno) method[63] together with a preconditioning method based on source field illumination[64], which could provide important information about the inverse of the second-order gradient[65]. We used a least-squares objective function[60] that is highly nonlinear and prone to cycle skipping[66]. To tackle this issue, in addition to starting from the streamer tomography model, we applied data time windowing[60] and frequency-continuation strategies[67].

The downward-extrapolated MCS dataset shows coherent early P-wave arrivals, including wide-angle refractions and reflections, and rarely shows P-to-S converted waves (Supplementary Figs. 1–3). Seafloor scattering is largely collapsed by the extrapolation but still hinders the exploitation of near-offset reflections. Hence, we designed time windows to select only early P-wave arrivals, starting immediately before first arrivals, with length of 1 s or shorter to exclude any water waves (direct, seafloor reflection). These time windows were used for all FWI steps. In addition, we implemented the frequency-continuation strategy[67] by sequentially inverting seismic data between 3 and 6 Hz, 3 and 9 Hz, and 3 and 14 Hz.

The waveform modelling was performed on a regular grid spaced at 12.5 m, with a time step of 1 ms. The initial V_P model for the first FWI stage was extracted from the streamer tomography model, and the initial V_S and density models were related to V_P using empirical relationships[68]. For later FWI stages with higher-frequency data, the best-fitting model results from the previous step were used as starting models. During the FWI iterations, both V_P and V_S models were updated, whereas the density model was always linked to V_P using the empirical relationship[68]. This is consistent with the dominance of wide-angle P-wave refractions in the windowed seismic data, which are relatively insensitive to fine-scale density model structures. Although the medium-wavelength V_S structure variation is required to better fit the wide-angle P-wave reflection amplitudes and reduce artefacts in the V_P model results, we do not interpret the FWI V_S models in this study because the V_S model results are less reliable than the V_P model results due to the lack of S-wave phases in the MCS data.

For each stage, we ran the FWI twice with different initial source signatures. The first run started from a band-limited spike function and updated it at every fifth iteration of velocity model update[69], concluding after 30 iterations. Then the second FWI run was reinitiated using the starting velocity models and the inverted source signature from the first run to update only velocities for 30 iterations. To avoid overfitting data noise, we utilized the L-curve method to select the most suitable model, balancing data misfit reduction and model roughness increment.

We present the 2D multi-scale FWI results on three MCS profiles (112, 114 and 113) covering the massif centre and three known hydrothermal fields. More-detailed model structures emerge with higher-frequency data (Extended Data Fig. 1 and Supplementary Figs. 5 and 6). The final FWI models are validated by the significant improvement in waveform fitting (Extended Data Fig. 2 and Supplementary Figs. 7 and 8). The size (sample by sample summation of the squared amplitude within each shot gather) of final residuals is much smaller than the size of the initial residuals (modelled with tomography-derived initial models and inverted 3–14 Hz source signatures) and the observed data size. The cross-correlation coefficients between modelled and observed shot gathers are significantly improved through the FWI, mostly exceeding 0.7 for the final models. These improvements, along with visual examination of observed and modelled shot gathers (for example, Supplementary Figs. 1–3), confirm that the final FWI models are close to the globally optimum solutions and largely free of cycle-skipping issues.

FWI resolution tests

We utilized chequerboard tests to evaluate the FWI model resolution, which is linked to seismic wavelength. To estimate the highest resolution limit, we conducted chequerboard tests based on the starting models and source signature used in the final FWI stage of 3–14 Hz data. The V_P models were perturbed by alternating positive and negative anomalies with amplitude of 5% and various dimensions. Synthetic data generated from perturbed models were combined with 20% band-limited (3–14 Hz) Gaussian noise. The FWI of the noisy synthetic data started from the unperturbed models, with the same parameters as in the last stage of field data inversion.

Three chequerboard patterns are examined, with horizontal × vertical anomaly dimensions (half wavelength) of (I) 750 m × 500 m, (II) 375 m × 375 m and (III) 250 m × 200 m. The results for profiles 112, 114 and 113, presented in Extended Data Fig. 3 and Supplementary Figs. 9 and 10, respectively, indicate that the patterns I and II can be well recovered throughout the Rainbow massif, whereas the pattern III can be recovered only within low-V_P (<6 km s^{-1}) regions. This is consistent with the theoretical resolution limit corresponding to a half wavelength of seismic wavefield. These tests demonstrate that the interpreted features are resolvable in our FWI results.

Local earthquake tomography

We inverted for the 3D V_P and V_S structure of the study region using the local earthquake tomography (LET) method LOTOS[70] and a

microearthquake catalogue obtained from recordings on 13 OBSs deployed during a period of ~9 months (May 2013–January 2014) on and around the Rainbow massif[18] (Extended Data Fig. 6). The full catalogue consists of hypocentres for 58,919 events. We extracted a subset of data by selecting only the best constrained events located within a 17 km × 18 km area between 36° 08.384–18.097′ N and 33° 47.255–58.627′ W. The criteria were (1) event depth is 10 km below sea level; (2) event root-mean squared travel-time residual is <0.2 s; (3) event must have at least four P-wave and four S-wave travel-time picks. The selected catalogue consisted of 15,496 events with 113,071 and 149,678 P-wave and S-wave arrival times, respectively (Extended Data Fig. 6).

LOTOS solves the ray-tracing problem using the ray-bending method[71] and solves simultaneously for event location and the 3D V_P and V_S structure using a regularized nonlinear tomographic inversion[70]. In the inversion, we chose smoothing and damping weights guided by previous similar studies[16,72] and by exploring trade-offs between data misfit and model roughness in chequerboard tests.

We derived a starting 1D V_P model from averaging the controlled-source OBS travel-time tomography model[11] in a 3-km-radius region centred on the Rainbow HF (Supplementary Fig. 11a). The starting 1D V_S structure was obtained from applying a V_P/V_S function to the starting V_P model. Tests showed that solutions were sensitive to the starting V_S model (and therefore, starting V_P/V_S model). To mitigate bias from a specific starting model choice, we followed a Monte Carlo approach (for example, ref. 73). We conducted a large number of inversions ($N = 100$), each with a different, randomly chosen starting 1D V_S model. The P-wave and S-wave arrival times of the microseismicity catalogue are consistent with an average V_P/V_S value of 2.05 for the whole region[18]. However, it is known that the V_P/V_S structure of oceanic crust varies with depth, with high values near the seafloor rapidly decreasing to typical values of 1.75–1.88 within the upper hundreds of metres[74–79]. Thus, we constructed the 100 starting V_P/V_S structures as 2-layer models (Supplementary Fig. 11b). The thickness of the upper layer was chosen from a uniform random distribution between 0.2 and 1.0 km; the lower-layer V_P/V_S value was constant and chosen from a uniform random distribution between 1.7 and 2.3; and the upper-layer V_P/V_S value decreases linearly from a seafloor value (chosen from a uniform random distribution between the lower-layer V_P/V_S value and 3.5) to the lower-layer V_P/V_S value. Typically, significant reduction in data misfit is achieved in two to three iterations. Thus, all inversions were run for five iterations, achieving a misfit reduction by 55–80% (Supplementary Fig. 12). The presented preferred V_P/V_S model (Fig. 2d and Extended Data Figs. 4d and 5d) is the average of the 100 solutions, and the standard deviation of all the solutions is taken as an estimate of the V_P/V_S model uncertainty (Supplementary Fig. 13).

The V_P/V_S model resolution was assessed through chequerboard tests. The input perturbation models consist of variations in V_P/V_S with an amplitude of 0.3, varying either laterally or vertically. Synthetic P-wave and S-wave travel times were generated from those models with the geometry identical to the field data. We present the recovered model anomalies from four chequerboard tests containing laterally varying perturbations with an anomaly dimension of 2 km × 2 km (Supplementary Fig. 15a–d) and with an anomaly dimension of 1 km × 1 km (Supplementary Fig. 15e–h); and vertically varying perturbations with an anomaly dimension of 2 km (Supplementary Fig. 15i) and 1 km (Supplementary Fig. 15j). These results indicate that lateral variations with a half wavelength of 2 km can be well resolved across the Rainbow massif at depth above ~4 km b.s.f., whereas around the centre of the massif and the hydrothermal fields, lateral variations with a half wavelength of 1 km can also be resolved. Vertical resolution is best within ~3 km of the model centre, where variations with a half wavelength of 1 km can be well resolved up to ~3 km b.s.f., while variations with a half wavelength of 2 km are resolved up to 4 km b.s.f.

Seismic properties and lithology

To discriminate between the seismic properties of gabbro and those of more olivine/serpentine-rich lithologies, we compiled laboratory measurements of samples obtained predominately through ocean deep drilling into gabbro and ultramafic rocks[80–82], along with a few serpentinite samples from seafloor dredges and ophiolites[83–85]. Measurements under confining pressure between 50 and 200 MPa are considered, corresponding to approximately 1–6 km b.s.f. The relevant lithologies are categorized into five groups: gabbro/gabbronorite (with <2% olivine), olivine/troctolitic gabbro (2–25% olivine), troctolite (14–28% olivine), serpentinite and dry ultramafic rocks (Extended Data Fig. 7). Statistical analysis indicates that V_P/V_S for gabbro/gabbronorite is mostly (95%) below 1.830, and entirely below 1.845, with a maximum likelihood at 1.780. The olivine/troctolitic gabbro has slightly higher V_P/V_S, with a maximum likelihood at 1.820 and a maximum value of 1.875. Together, these two groups of gabbroic rocks have 95% of V_P/V_S values below 1.85. For serpentinite, the V_P/V_S is mostly (95%) larger than 1.85. Troctolite has V_P/V_S values almost evenly distributed between 1.81 and 1.94, but their abundance in the drilled gabbroic cores is much less than that of gabbroic rocks; for example, troctolite groups account for 8.1% of lithologies, whereas gabbro groups account for 88% in the 1.4-km-deep hole drilled into the core of the Atlantis massif[86]. In this study, we selected $V_P/V_S = 1.85$ as a reference value to distinguish between gabbro and serpentinite, where the 95% confidence level of gabbroic V_P/V_S distribution and the 5% confidence level of serpentinite V_P/V_S distribution coincide (Extended Data Fig. 7d).

On the basis of the preceding considerations, the LET-derived V_P/V_S variations provide robust constraints on long-wavelength lithology variations, indicating a larger concentration of gabbro at the core of the Rainbow massif. In addition, the higher-resolution FWI V_P models aid in delineating sharp lithological boundaries. The laboratory measurements show that gabbro's V_P values are generally >6.3 km s^{-1} (Extended Data Fig. 7a). However, the macro-scale measurements, such as sonic log and MCS experiment, would observe lower velocities than the micro-scale lab measurements. We refer to the studies of the Atlantis massif, where its gabbroic core has been studied using both drilling and FWI of downward-extrapolated MCS data[14,32]. These studies indicate that the intact gabbro core's V_P is generally larger than 6 km s^{-1}, which may be sharply lowered to 5–6 km s^{-1} by deformation and alteration at the surficial hundreds of metres and within certain internal sections, where more olivine-rich lithologies locally dominate[14]. Our FWI models reveal similar sharp transitions across 5–6 km s^{-1} around the high-V_P core (Fig. 2c). Consequently, we can further constrain the identification of the parts of our models dominated by gabbroic intrusions using $V_P > 5.5$ km s^{-1} as an additional discriminant. Due to the sharpness of transitions imaged by the FWI, selecting different V_P values in the 5–6 km s^{-1} range has only a minor effect on delineating the gabbro-dominant region.

In summary, gabbro intrusions can be confidently interpreted in our models using $V_P > 5.5$ km s^{-1} and $V_P/V_S < 1.85$ as delineating criteria. This delineation reveals a gabbro-dominant region in the core of the Rainbow massif at shallow depths (grey shaded regions in Fig. 2 and Extended Data Figs. 4 and 5).

Porosity and serpentinization estimates

We calculated the fine-scale porosity structure and extent of serpentinization of the Rainbow massif by comparing the FWI V_P and the LET V_P/V_S values with predictions from effective medium theory (EMT)[87] (Extended Data Fig. 8). Effective moduli for a two-phase media are computed assuming a background matrix consisting of serpentinized peridotite with serpentine fraction s, with a porosity c of brine-filled inclusions of aspect ratio α. Shear (μ_0) and bulk (K_0) moduli for the background matrix are calculated using laboratory measurements in serpentinized samples relating density (ρ_0), compressional (V_{P0}) and

shear (V_{S0}) wave velocity to serpentine fraction[82] and relationships between seismic velocities and isotropic elastic moduli:

$$\rho_0[\mathrm{kg\,m^{-3}}] = -890 \times s + 3,340 \quad (1)$$

$$V_{P0}[\mathrm{m\,s^{-1}}] = -2,858 \times s + 7,931 \quad (2)$$

$$V_{S0}[\mathrm{m\,s^{-1}}] = -1,921.6 \times s + 4,277 \quad (3)$$

$$\mu_0 = V_{S0}^2 \times \rho_0 \quad (4)$$

$$K_0 = V_{P0}^2 \times \rho_0 - \frac{4}{3}\mu_0 \quad (5)$$

For the inclusions, we use the following properties: $\rho' = 1{,}030\ \mathrm{kg\,m^{-3}}$; $\mu' = 0$ GPa; $K' = 2.5$ GPa (ref. 88).

In the case of a matrix lithology consisting of unaltered peridotite, the majority of our observations can be explained by some combination of c and α (Extended Data Fig. 8a). However, if serpentinization of the matrix is included, only a portion of our [V_P, V_P/V_S] pairs can be explained by the EMT model. For example, for a 50% serpentinization, only data points with $V_P < 6.5\ \mathrm{km\,s^{-1}}$ are consistent with the model (Extended Data Fig. 8b). If full serpentinization is assumed, only data points with V_P less than ~5 km s^{-1} and V_P/V_S greater than ~2 are consistent with the model (Extended Data Fig. 8c). These examples illustrate that although EMT solutions are non-unique, some portions of our seismic velocity models are consistent only with a narrow range of properties (for example, all data points with $V_P > 7.4\ \mathrm{km\,s^{-1}}$ require a background matrix <20% serpentinized) while other portions are consistent with any degree of serpentinization (for example, $V_P < 5\ \mathrm{km\,s^{-1}}$ and $V_P/V_S > 2$).

Despite the non-uniqueness, we can explore endmember structures with the minimum and maximum extents of serpentinization that are consistent with our results. The endmember case with minimum serpentinization is trivial and is derived from EMT solutions in Extended Data Fig. 8a. It assumes that the massif consists exclusively of unaltered peridotite (except where the gabbro-dominant region is interpreted) with low porosity of ~2–4% in the upper ~1.5 km and negligible below, and smallest pore aspect ratio (Extended Data Fig. 9g–i). Alternatively, the endmember solution that allows for the maximum extent of serpentinization is built iteratively from EMT solutions spanning values of s between 0% and 100% at 1% increments. We start by determining c and α with $s = 100\%$ for [V_P, V_P/V_S] values that have an EMT solution, which locate in the upper few 100s of metres b.s.f. (Extended Data Fig. 9c). We then proceed to determine c and α with $s = 99\%$ (which generally map into data points slightly deeper than the previous iteration), then $s = 98\%$ and so forth until $s = 0\%$, which fills in the deepest portions where V_P is highest. This results in a porosity structure consisting of high porosity in the upper ~1 km rapidly decreasing with depth and including high-porosity regions along the FWI-imaged low-V_P channels (Extended Data Fig. 9a). The serpentinization structure shows a fully serpentinized Rainbow massif in the upper ~1 km, with serpentinization progressively decreasing with depth and including high-serpentinization regions (60–80%) along the low-V_P channels (Extended Data Fig. 9c). The pore aspect ratio is 0.01–0.10 at depth <2 km b.s.f. (Extended Data Fig. 9b). Solutions between these two endmember models exist and are consistent with our velocity models, for example, solution with the maximum extent of serpentinization capped at 50% (Extended Data Fig. 9d–f).

Data availability

The MCS raw data are archived with the IEDA Marine Geoscience Data System (https://doi.org/10.1594/IEDA/320244). The OBS data are archived at the IRIS Data Management Center under code X3 (https://www.fdsn.org/networks/detail/X3_2013). The local earthquake catalogue and travel-time data used in this study are available at figshare (https://doi.org/10.6084/m9.figshare.25484716)[89]. Source data are provided with this paper. Seismic models and derived rock properties are provided in the source data files associated with Fig. 2 and Extended Data Figs. 4 and 5.

Code availability

The LOTOS code for local earthquake tomography is publicly accessible (http://www.ivan-art.com/science/LOTOS/). Other codes are available upon request from the corresponding authors.

References

51. Canales, J. et al. MARINER: seismic investigation of the Rainbow hydrothermal field and its tectono/magmatic setting, Mid-Atlantic Ridge 36° 14' N—a report from RV *MG Langseth* Cruise MGL1305. *InterRidge N.* **22**, 46–52 (2013).
52. Harding, A. J., Kent, G. M., Blackman, D. K., Singh, S. & Canales, J. P. A new method for MCS refraction data analysis of the uppermost section at a Mid-Atlantic Ridge core complex. *Eos. Trans.* **88**, abstr. S12A–03 (2007).
53. Arnulf, A. F., Singh, S. C., Harding, A. J., Kent, G. M. & Crawford, W. Strong seismic heterogeneity in layer 2A near hydrothermal vents at the Mid-Atlantic Ridge. *Geophys. Res. Lett.* **38**, L13320 (2011).
54. Arnulf, A. F., Harding, A. J., Singh, S. C., Kent, G. M. & Crawford, W. C. Nature of upper crust beneath the Lucky Strike volcano using elastic full waveform inversion of streamer data. *Geophys. J. Int.* **196**, 1471–1491 (2014).
55. Berryhill, J. R. Wave-equation datuming before stack. *Geophysics* **49**, 2064–2066 (1984).
56. Van Avendonk, H. J. A., Shillington, D. J., Holbrook, W. S. & Hornbach, M. J. Inferring crustal structure in the Aleutian island arc from a sparse wide-angle seismic data set. *Geochem. Geophys. Geosyst.* **5**, Q08008 (2004).
57. Moser, T. J. Shortest path calculation of seismic rays. *Geophysics* **56**, 59–67 (1991).
58. Paige, C. C. & Saunders, M. A. LSQR: an algorithm for sparse linear equations and sparse least squares. *ACM Trans. Math. Softw.* **8**, 43–71 (1982).
59. Balay, S. et al. *PETSc/TAO Users Manual* (Argonne National Laboratory, 2023); https://doi.org/10.2172/1968587
60. Shipp, R. M. & Singh, S. C. Two-dimensional full wavefield inversion of wide-aperture marine seismic streamer data. *Geophys. J. Int.* **151**, 325–344 (2002).
61. Levander, A. R. Fourth-order finite-difference *P-SV* seismograms. *Geophysics* **53**, 1425–1436 (1988).
62. Tarantola, A. Inversion of seismic reflection data in the acoustic approximation. *Geophysics* **49**, 1259–1266 (1984).
63. Liu, D. C. & Nocedal, J. On the limited memory BFGS method for large scale optimization. *Math. Program.* **45**, 503–528 (1989).
64. Plessix, R.-E. & Mulder, W. A. Frequency-domain finite-difference amplitude-preserving migration. *Geophys. J. Int.* **157**, 975–987 (2004).
65. Métivier, L. & Brossier, R. The SEISCOPE optimization toolbox: a large-scale nonlinear optimization library based on reverse communication. *Geophysics* **81**, F1–F15 (2016).
66. Virieux, J. & Operto, S. An overview of full-waveform inversion in exploration geophysics. *Geophysics* **74**, WCC1–WCC26 (2009).
67. Bunks, C., Saleck, F. M., Zaleski, S. & Chavent, G. Multiscale seismic waveform inversion. *Geophysics* **60**, 1457–1473 (1995).
68. Brocher, T. M. Empirical relations between elastic wavespeeds and density in the Earth's crust. *Bull. Seismol. Soc. Am.* **95**, 2081–2092 (2005).
69. Pratt, R. G. Seismic waveform inversion in the frequency domain: part 1, theory and verification in a physical scale model. *Geophysics* **64**, 888–901 (1999).

70. Koulakov, I. LOTOS code for local earthquake tomographic inversion: benchmarks for testing tomographic algorithms. *Bull. Seismol. Soc. Am.* **99**, 194–214 (2009).
71. Moser, T. J., Nolet, G. & Snieder, R. Ray bending revisited. *Bull. Seismol. Soc. Am.* **82**, 259–288 (1992).
72. Koulakov, I. et al. Unrest of the Udina volcano in Kamchatka inferred from the analysis of seismicity and seismic tomography. *J. Volcanol. Geotherm. Res.* **379**, 45–59 (2019).
73. Korenaga, J. et al. Crustal structure of the southeast Greenland margin from joint refraction and reflection seismic tomography. *J. Geophys. Res. Solid Earth* **105**, 21591–21614 (2000).
74. Au, D. & Clowes, R. M. Shear-wave velocity structure of the oceanic lithosphere from ocean bottom seismometer studies. *Geophys. J. Int.* **77**, 105–123 (1984).
75. Christeson, G. L., Shaw, P. R. & Garmany, J. D. Shear and compressional wave structure of the East Pacific Rise, 9°–10° N. *J. Geophys. Res. Solid Earth* **102**, 7821–7835 (1997).
76. Harmon, N., Forsyth, D. & Webb, S. Using ambient seismic noise to determine short-period phase velocities and shallow shear velocities in young oceanic lithosphere. *Bull. Seismol. Soc. Am.* **97**, 2009–2023 (2007).
77. Kim, E. et al. Upper crustal *Vp*/*Vs* ratios at the Endeavour segment, Juan de Fuca Ridge, from joint inversion of P and S traveltimes: implications for hydrothermal circulation. *Geochem. Geophys. Geosyst.* **20**, 208–229 (2019).
78. McClymont, A. F. & Clowes, R. M. Anomalous lithospheric structure of Northern Juan de Fuca plate—a consequence of oceanic rift propagation? *Tectonophysics* **406**, 213–231 (2005).
79. Vera, E. E. et al. The structure of 0- to 0.2-m.y.-old oceanic crust at 9°N on the East Pacific Rise from expanded spread profiles. *J. Geophys. Res. Solid Earth* **95**, 15529–15556 (1990).
80. Iturrino, G. J., Miller, D. J. & Christensen, N. I. Velocity behavior of lower crustal and upper mantle rocks from a fast-spreading ridge at Hess Deep. *Proc. Ocean Drill. Program Sci. Results* **147**, 417–440 (1996).
81. Iturrino, G. J., Christensen, N. I., Kirby, S. & Salisbury, M. H. Seismic velocities and elastic properties of oceanic gabbroic rocks from hole 735B. *Proc. Ocean Drill. Program Sci. Results* **118**, 227–244 (1991).
82. Miller, D. J. & Christensen, N. I. Seismic velocities of lower crustal and upper mantle rocks from the slow-spreading Mid-Atlantic Ridge, south of the Kane Transform Zone (MARK). *Proc. Ocean Drill. Program Sci. Results* **153**, 437–456 (1997).
83. Christensen, N. I. Elasticity of ultrabasic rocks. *J. Geophys. Res.* **71**, 5921–5931 (1966).
84. Christensen, N. I. The abundance of serpentinites in the oceanic crust. *J. Geol.* **80**, 709–719 (1972).
85. Christensen, N. I. Ophiolites, seismic velocities and oceanic crustal structure. *Tectonophysics* **47**, 131–157 (1978).
86. Blackman, D. et al. Integrated Ocean Drilling Program Expedition 305 preliminary report oceanic core complex formation, Atlantis massif oceanic core complex formation, Atlantis massif, Mid-Atlantic Ridge: drilling into the footwall and hanging wall of a tectonic exposure of deep, young oceanic lithosphere to study deformation, alteration, and melt generation. In *Proc. Int. ocean Drill. Program* Vol. 305 (eds Blackman, D.K. et al.) 1–78 (IODP, 2005).
87. Kuster, G. T. & Toksöz, M. N. Velocity and attenuation of seismic waves in two-phase media: part I. Theoretical formulations. *Geophysics* **39**, 587–606 (1974).
88. Toksöz, M. N., Cheng, C. H. & Timur, A. Velocities of seismic waves in porous rocks. *Geophysics* **41**, 621–645 (1976).
89. Canales, J. P. Local earthquake tomography data from the Rainbow massif, Mid-Atlantic Ridge. *figshare* https://doi.org/10.6084/m9.figshare.25484716 (2024).

Acknowledgements

We are grateful to the captain, crew, technical staff and science party of the R/V *M. G. Langseth* leg MGL1305 and the R/V *Pelagia* leg 64PE382, and the NSF-funded Ocean Bottom Seismic Instrument Center (formerly OBSIP, https://obsic.whoi.edu) team. We thank R. Sohn for providing the microseismicity catalogue. This work was supported by the NSF grant OCE-2001012 to J.P.C. and H.J. Data acquisition was supported by NSF grants OCE-0961680 and OCE-0961151 to J.P.C. and R.D. H.J. was partially supported by the Ocean Frontier Institute International Postdoctoral Fellowship Program of Dalhousie University in partnership with Woods Hole Oceanographic Institution.

Author contributions

H.J. performed the multichannel seismic data processing and modelling, interpreted the results, wrote the manuscript and acquired funding. J.P.C. co-led the data acquisition, conducted the local earthquake tomography and effective medium modelling, interpreted the results, wrote the manuscript and acquired funding. R.D. co-led the data acquisition, provided the controlled-source ocean-bottom seismometer tomography model and revised the manuscript. M.R.N. revised the manuscript and acquired funding.

Competing interests

The authors declare no competing interests.

Additional information

Extended data is available for this paper at https://doi.org/10.1038/s41561-024-01444-y.

Supplementary information The online version contains supplementary material available at https://doi.org/10.1038/s41561-024-01444-y.

Correspondence and requests for materials should be addressed to Hanchao Jian or J. Pablo Canales.

Peer review information *Nature Geoscience* thanks Stephen Hicks, Toshio Nozaka and Sven Petersen for their contribution to the peer review of this work. Primary Handling Editor: Alireza Bahadori, in collaboration with the *Nature Geoscience* team.

https://doi.org/10.1038/s41561-024-01444-y

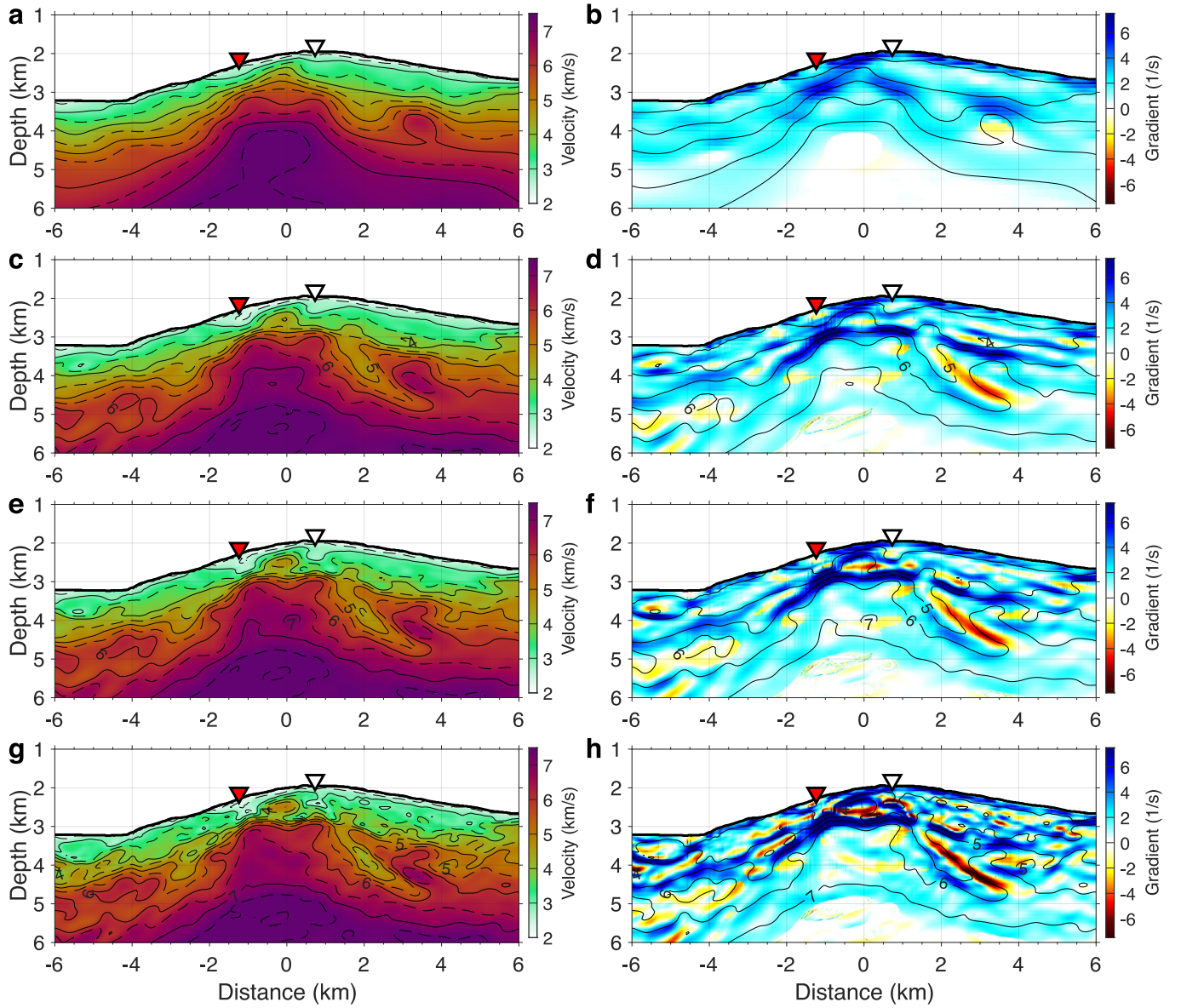

Extended Data Fig. 1 | V_P model evolution through the streamer tomography and full waveform inversion (FWI) of profile 112. a and **b**, V_P model and spatial gradients after the streamer traveltime tomography; **c** and **d**, after FWI of 3-6 Hz data; **e** and **f**, after FWI of 3-9 Hz data; **g** and **h**, after FWI of 3-14 Hz data, same as shown in Fig. 2. Models in **a**, **c** and **e** are used as starting models in following stages that result in models in **c**, **e** and **g**, respectively. Inverted triangles are projected locations of hydrothermal fields as shown in Fig. 1b.

https://doi.org/10.1038/s41561-024-01444-y

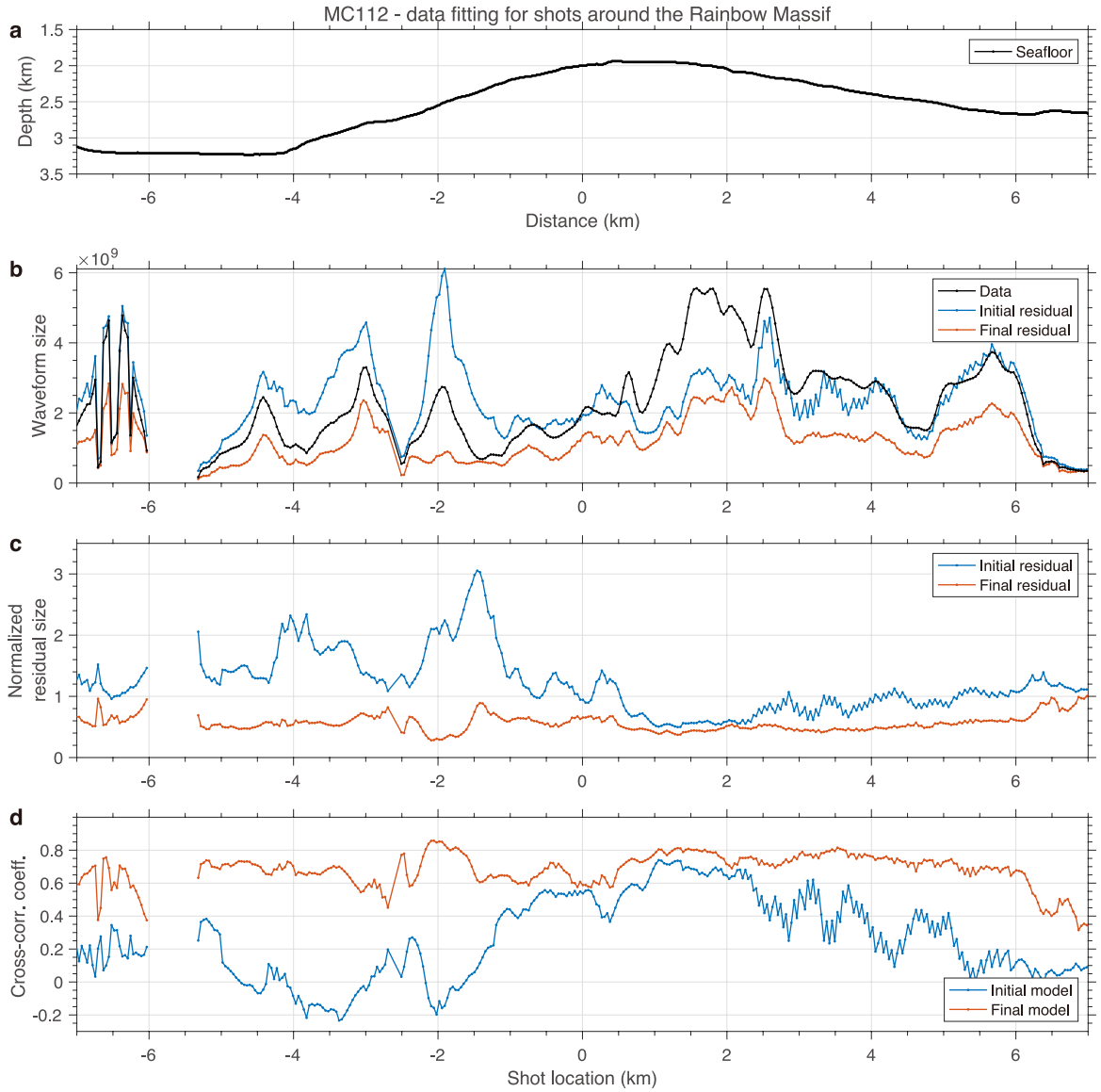

Extended Data Fig. 2 | Waveform data fitting along profile 112 around the Rainbow massif. a, Bathymetry along profile 112. **b**, Sum of squared amplitude within each windowed shot gather, for the observed data, initial residual (modeled with the tomography-derived starting model and inverted 3-14 Hz source signature) and final residual, respectively. **c**, The initial and final residual normalized by the observed data size. **d**, The cross-correlation coefficients between the observed and the initial model data and between the observed and final model data.

https://doi.org/10.1038/s41561-024-01444-y

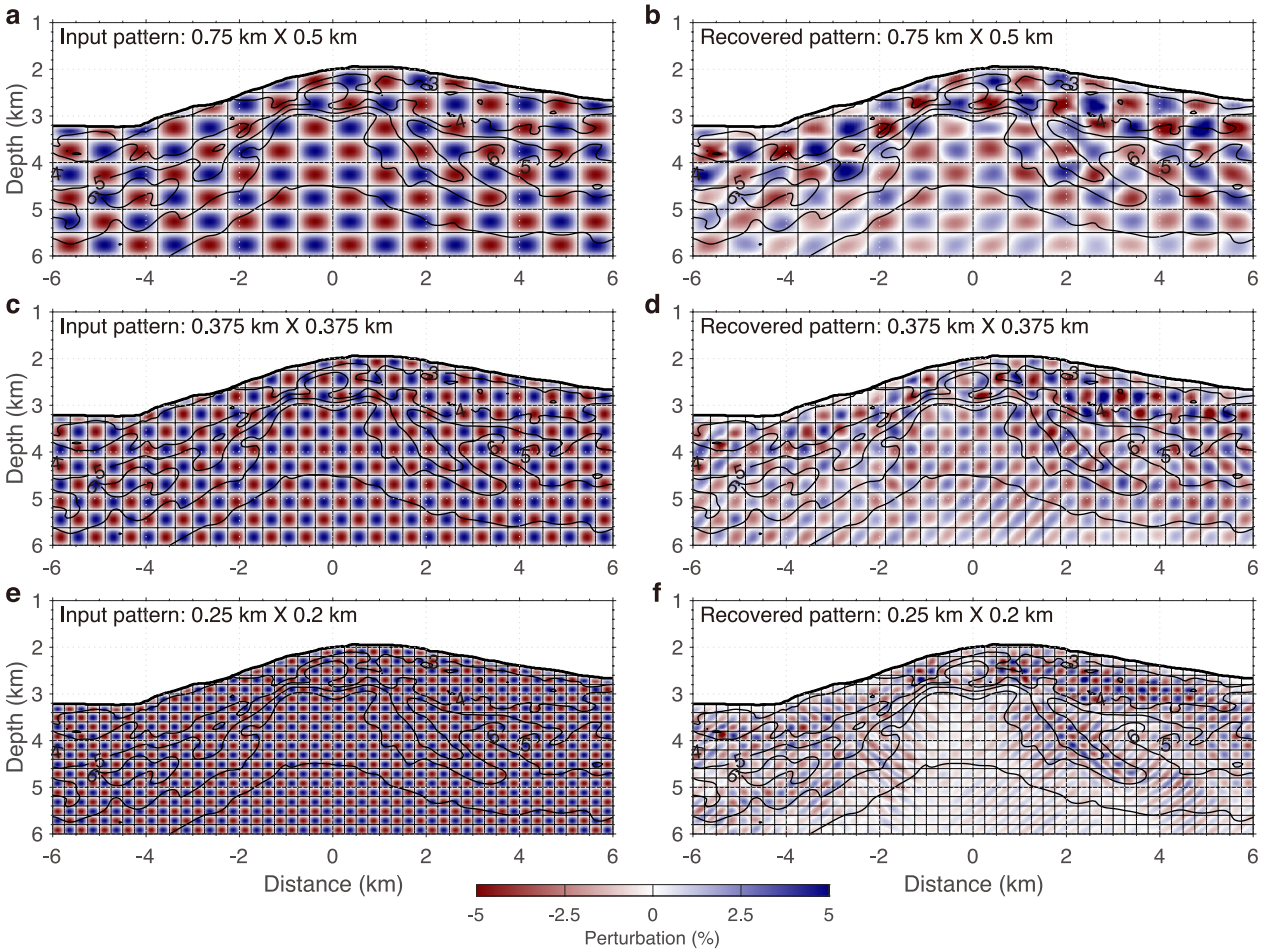

Extended Data Fig. 3 | Chequerboard tests for the full waveform inversion (FWI) of profile 112. a, **c** and **e**, Input chequerboard patterns with different anomaly size or half wavelength that are described in the plot. **b**, **d** and **f**, Recovered anomalies from the FWI of the noisy synthetic data generated using input patterns of **a**, **c** and **e**, respectively. Labeled contours are V_P from the final FWI model of field data (Fig. 2a).

https://doi.org/10.1038/s41561-024-01444-y

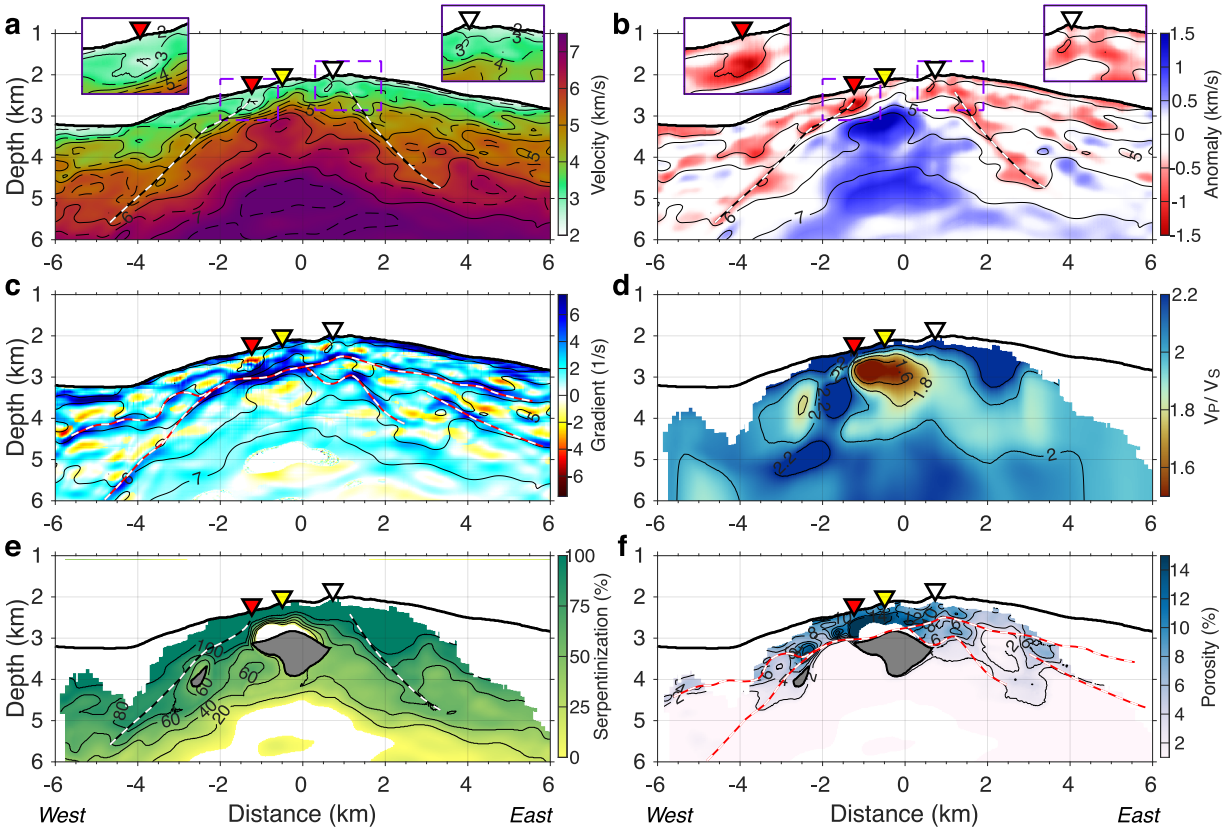

Extended Data Fig. 4 | Geophysical cross-sections along profile 114. a. V_P; **b**. V_P anomalies; and **c**. V_P gradients (amplitude of total spatial gradient combined with the sign of vertical gradient) derived from the full waveform inversion of multichannel seismic data. Labeled black contours in **a**-**c** all correspond to the V_P model in **a**. **d**. V_P/V_S ratios derived from the local earthquake tomography. Preferred estimates of, **e**. degree of serpentinization and, **f**. porosity from effective medium theory consistent with the [V_P, V_P/V_S] results in **a** and **d** (Methods). Inverted triangles are projected locations of hydrothermal fields as shown in Fig. 1b. The insets in **a** and **b** show zoomed-in plots of the shallow low-V_P zones associated with the hydrothermal fields. Black-white dashed lines in **a**, **b** and **e** delineate low-V_P channels as interpreted in **b**. Red-white dashed lines in **c** and **f** delineate high-V_P gradients as interpreted in **c**. The dark gray patches on **e** and **f** mark interpreted gabbro-dominant regions.

https://doi.org/10.1038/s41561-024-01444-y

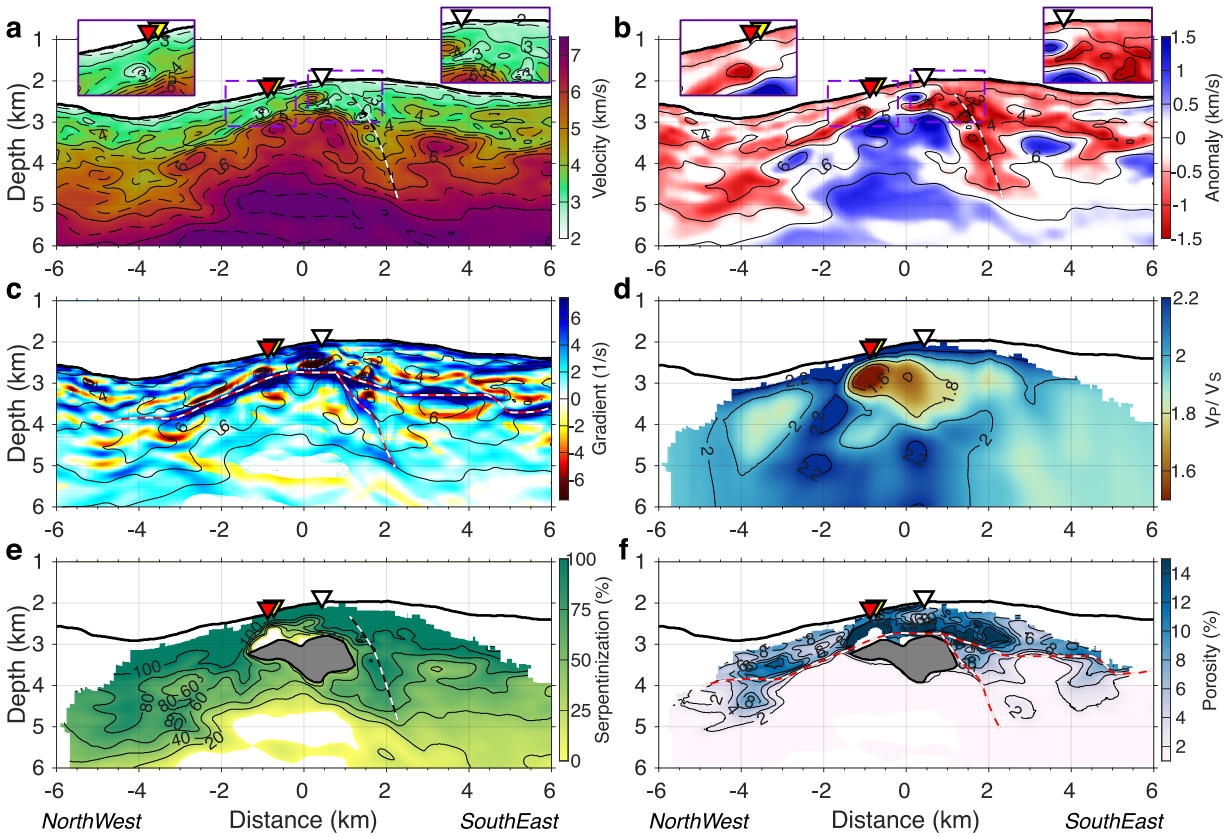

Extended Data Fig. 5 | Geophysical cross-sections along profile 113. a. V_P; **b**. V_P anomalies; and **c**. V_P gradients (amplitude of total spatial gradient combined with the sign of vertical gradient) derived from the full waveform inversion of multichannel seismic data. Labeled black contours in **a**-**c** all correspond to the V_P model in **a**. **d**. V_P/V_S ratios derived from the local earthquake tomography. Preferred estimates of, **e**. degree of serpentinization, and, **f**. porosity from effective medium theory consistent with the [V_P, V_P/V_S] results in **a** and **d** (Methods). Inverted triangles are projected locations of hydrothermal fields as shown in Fig. 1b. The insets in **a** and **b** show zoomed-in plots of the shallow low-V_P zones associated with the hydrothermal fields. Black-white dashed lines in **a**, **b** and **e** delineate low-V_P channels as interpreted in **b**. Red-white dashed lines in **c** and **f** delineate high-V_P gradients as interpreted in **c**. The dark gray patches on **e** and **f** mark interpreted gabbro-dominant regions.

https://doi.org/10.1038/s41561-024-01444-y

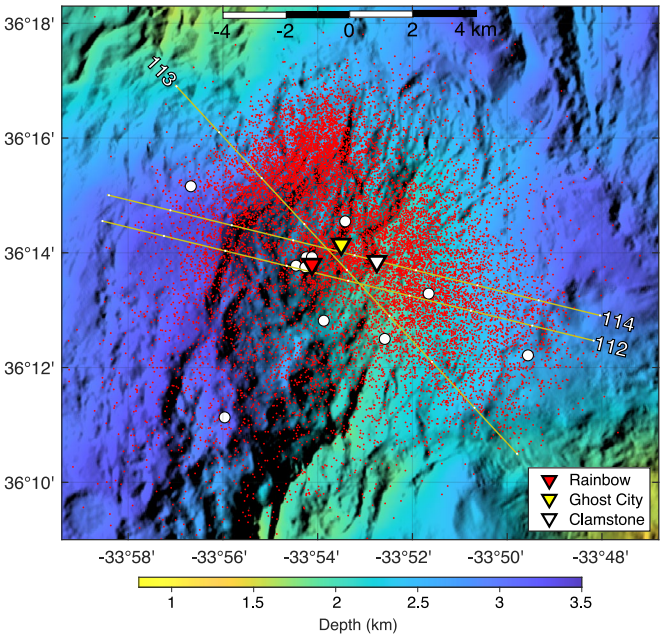

Extended Data Fig. 6 | Bathymetry and microseismicity of the Rainbow massif. Red dots represent relocated epicenters from a subset of the microseismicity catalog of ref. 18 used for 3-D local earthquake tomography (Methods). Open circles locate thirteen ocean bottom seismometers, six of which are clustered at the Rainbow hydrothermal field.

https://doi.org/10.1038/s41561-024-01444-y

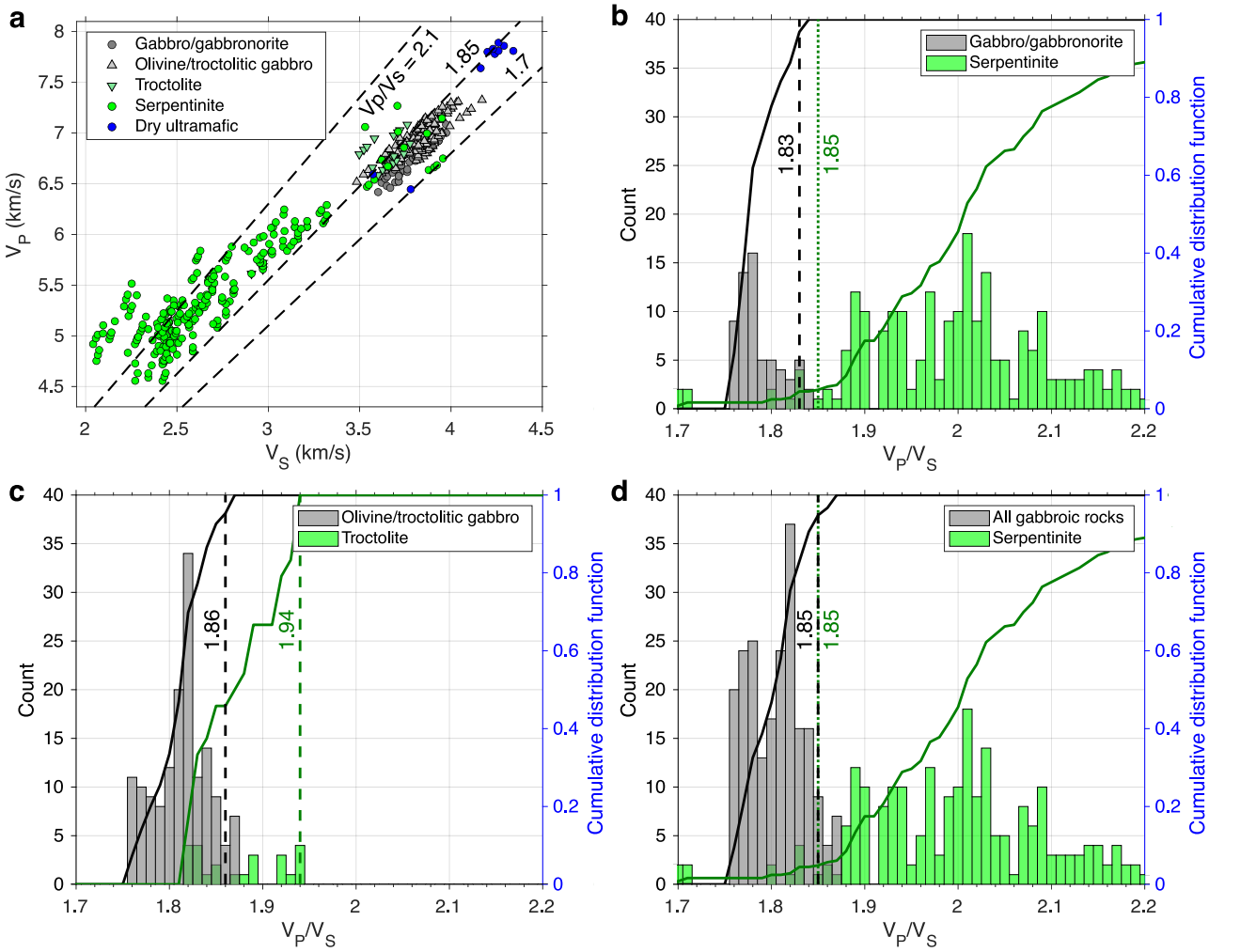

Extended Data Fig. 7 | Relationship of V_P/V_S ratio and lithology. The dataset is a compilation of results derived from laboratory measurements (see Methods for data source details). **a**, V_P versus V_S diagram with dashed lines denoting constant V_P/V_S values. **b-d**, Histograms of V_P/V_S values for different lithology groups. Solid curves represent cumulative distribution functions, with black curves for groups represented by gray histograms, and dark green curves for groups represented by green histograms. Vertical lines indicate the 95% confidence level (dashed lines) and the 5% confidence level (dotted lines), respectively.

https://doi.org/10.1038/s41561-024-01444-y

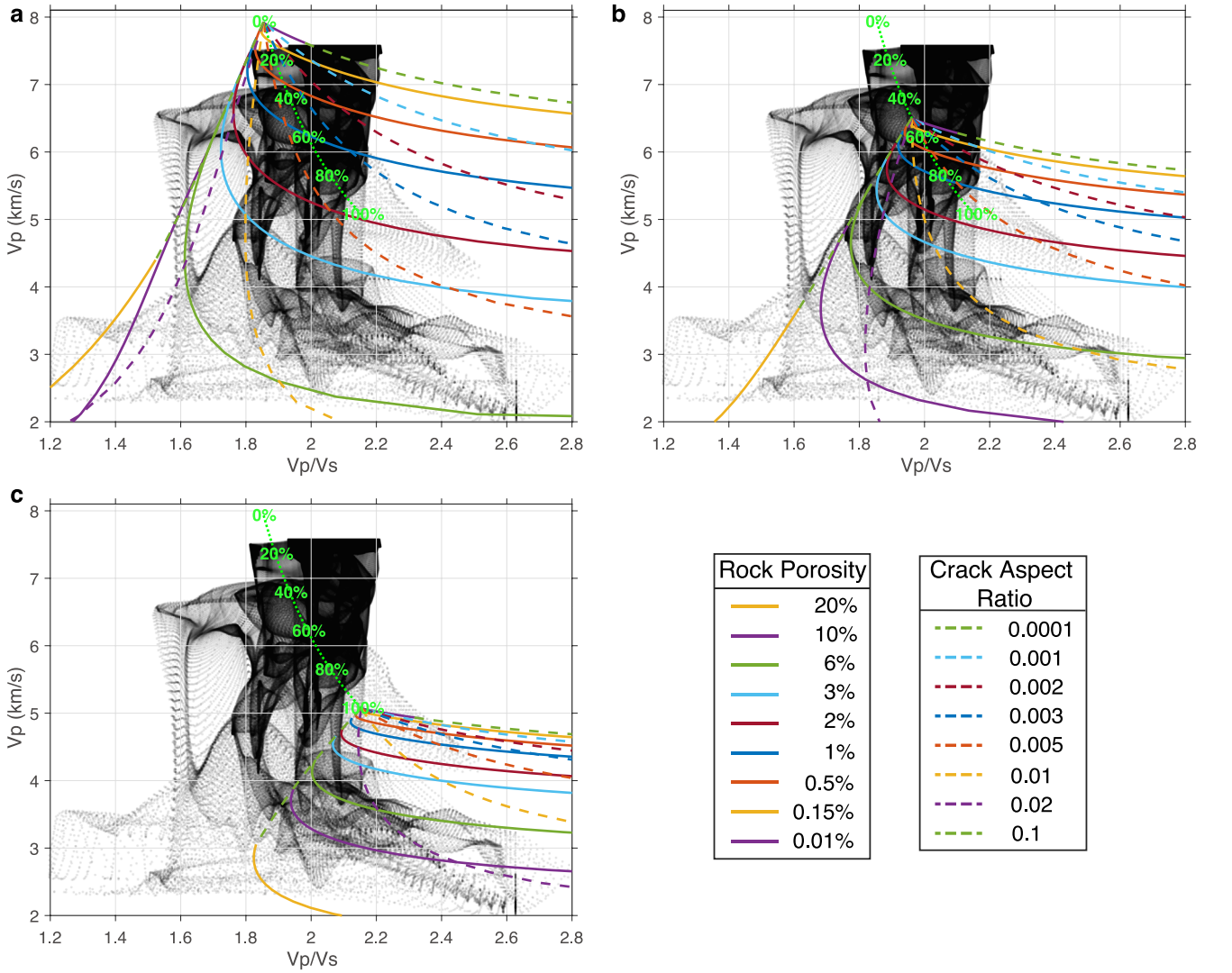

Extended Data Fig. 8 | V_P vs. V_P/V_S diagrams and effective medium theory predictions. Scatter plot of the full waveform inversion (FWI) V_P and local earthquake tomography (LET) V_P/V_S model values. Multi-colored curves represent effective medium theory (EMT) predictions of V_P and V_P/V_S as a function of porosity for a given aspect ratio (dashed lines), or as a function of aspect ratio for a given porosity (solid lines). Dotted green lines with labels correspond to predictions for a non-porous peridotite as a function of serpentinization fraction[82] (labeled in 20% increments). Rock matrix is **a**, unaltered peridotite; **b**, 50% serpentinized peridotite; **c**, fully serpentinized peridotite.

https://doi.org/10.1038/s41561-024-01444-y

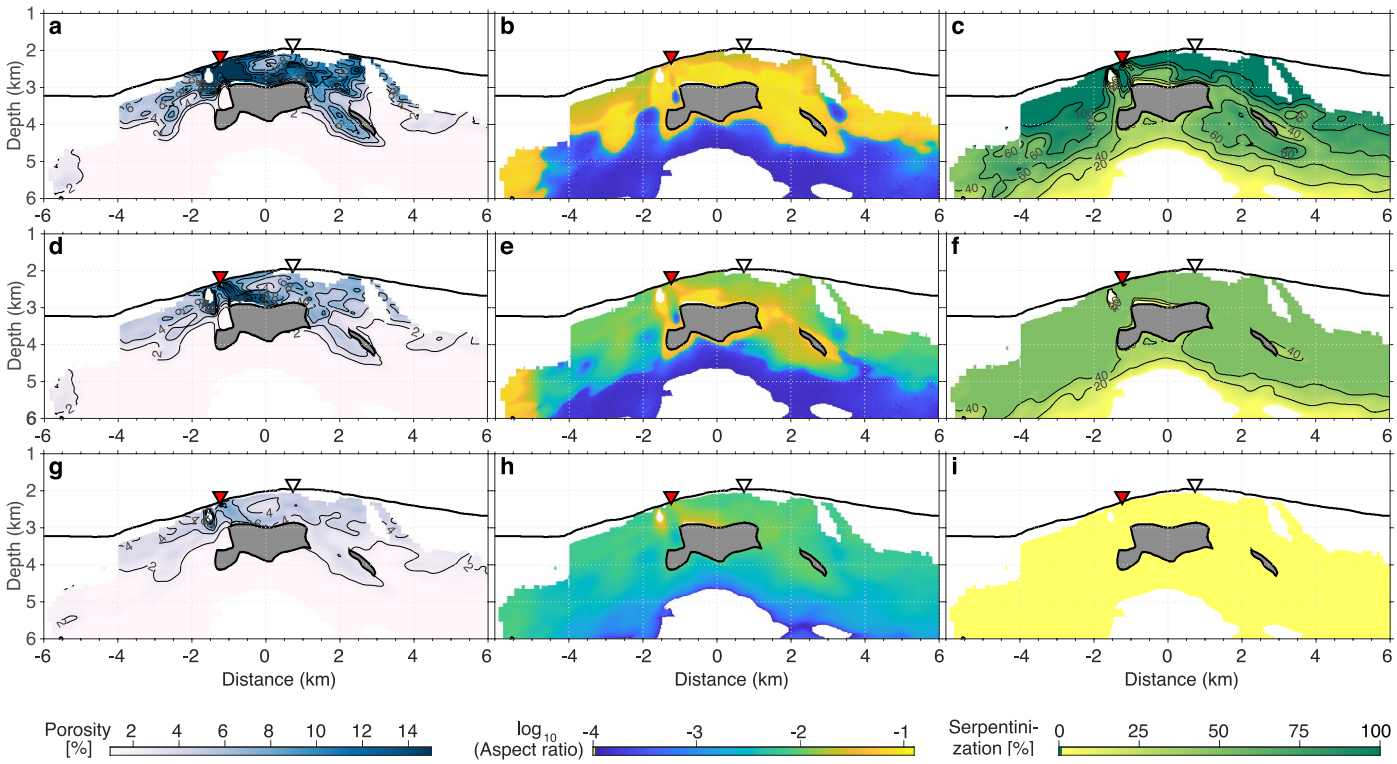

Extended Data Fig. 9 | Estimates of porosity, crack aspect ratio, and extent of serpentinization along profile 112. a-c, Endmember models in which the matrix rock is allowed to reach the maximum extent of serpentinization (up to 100%). **d-f**, Intermediate models in which the maximum extent of serpentinization is limited at 50%. **g-i**, Endmember models in which the matrix rock is forced to be unaltered peridotite (0% serpentinization).